RESEARCH ARTICLE

Key Points:
- Slickenlines form at 450°C but not 100°C in wet experiments, by brittle wear and solution-deposition
- They are slip vector-perpendicular undulations decorated by silica beads in an amorphous silica matrix
- Formation accompanies strain softening, fault smoothing, and maintenance of a constant slip direction

Striation and slickenline development on quartz fault surfaces at crustal conditions: Origin and effect on friction

Virginia G. Toy[1] (ID)**, André Niemeijer[2]** (ID)**, Francois Renard[3,4]** (ID)**, Luiz Morales[5]** (ID)**, and Richard Wirth[6]**

[1]Department of Geology, University of Otago, Dunedin, New Zealand, [2]Department of Geosciences, Utrecht University, Utrecht, Netherlands, [3]Department of Geosciences, PGP, University of Oslo, Oslo, Norway, [4]ISTerre, University Grenoble Alpes, Grenoble, France, [5]Scope METH Zürich, Zürich, Switzerland, [6]Helmholtz Centre Potsdam, GFZ German Research Centre for Geosciences, Potsdam, Germany

Abstract Fragments of optically flat silica discs embedded in synthetic gouge were deformed to examine the relationship between the development of striations and slickenlines, and deformation mechanisms, conditions, and fault rheology. Experiments were performed under hydrothermal conditions in a rotary shear apparatus at 100°C or 450°C, to shear strains of $2.02 < \gamma < 8.25$. Slip hardening and softening prevail at low and high temperatures, respectively. In recovered samples, disc fragment surfaces are decorated by fine gouge, sometimes arranged in trails, pits, and scratch marks. Prominent grooves —inferred slickenlines—with constant orientation, wavelength <10 µm, and amplitude <0.7 µm are only observed on disc fragments deformed at 450°C. Some parts of the grooves below the original disc fragment surface contain scattered rounded beads of silica ~200 nm diameter. Conversely, close examination of pits in 100°C experiments reveals they contain angular particles <2 µm diameter. The 200 nm diameter crystalline quartz can precipitate at 450°C in only 250 s, well within the time frame of the experiments but precipitation at 100°C would take at least 8 years. No systematic dislocation arrays were observed in the quartz disc fragments, but microfractures are sporadically present. This indicates that at both temperatures brittle failure generated microfractures and microcomminution occurred where gouge particles impacted disc fragment surfaces. These observations suggest formation of silica beads by precipitation from amorphous silica facilitates slip weakening, smoothing of the fault surface parallel to the slip vector, development of undulations perpendicular to the slip vector by a pressure solution creep mechanism, weakening, and maintenance of a constant slip direction.

1. Introduction

1.1. Slip Vector-Parallel Features on Faults

Slip vector-parallel lineations are commonly observed on natural fault surfaces. Past studies have focused on the information they can provide about kinematics of fault zones within which they are found [e.g., *Etchecopar et al.*, 1981; *Twiss et al.*, 1991; *Petit*, 1987; *Spörli and Anderson*, 1990]. *Means* [1987] suggested possible mechanisms of their formation are asperity plowing, debris streaking, erosional sheltering, fiber growth, and dissolution yielding slickolites (slip-parallel stylolites) and concluded that none of these mechanisms should yield ridge-and-groove striations commonly observed on fault surfaces and generated in paraffin wax experiments. *Engelder and Scholz* [1976] interpreted that "wear tracks" will form on surfaces impacted by asperities on the opposing surface by a combination of frictional wear and plastic deformation but did not present evidence of operation of the latter. Questions about the mechanisms of their development remain to the current day, perhaps because there have been only a few recent investigations of the conditions necessary for formation of these features in deforming systems or of the mechanical effects of their presence [e.g., *Kitamura et al.*, 2013]. Systematic studies of these aspects are required if we are to infer fault mechanics from observations of extinct structures.

Doblas [1998] defined 68 different types of slickenside (i.e., slip vector parallel) kinematic indicators that may be found on fault surfaces, but we prefer to use a simpler set of categories in this contribution. Hereinafter, slip vector-parallel lineations are categorized into one of three main morphologies: striations, slickenfibres, and slickenlines. We define *striations* as grooves scratched into fault surfaces as a consequence of brittle wear. They commonly decorate near-surface faults, such as the Itozawi Fault, which slipped to generate the M_w 6.6 Iwaki earthquake in 2011, Japan [*Otsubo et al.*, 2013], and the Alpine Fault principal slip zone, New Zealand [e.g., *Toy and Mitchell*, 2014].

Slickenfibres comprise new minerals precipitated on a fault surface in a fibrous habit, elongated parallel to the slip vector. They are observed within accretionary prism mélanges such as at Chrystals Beach, New Zealand [*Fagereng et al.*, 2011], and in the Shimanto belt, Japan [*Kitamura et al.*, 2005], and are common in fault-vein networks in orogenic belts exhumed from subgreenschist facies conditions, such as within prehnite-pumpellyite facies metasediments at Benmore Dam, New Zealand [*de Ronde et al.*, 2001].

Slickenlines are smooth polished features, with ridge and groove morphology, and reflective surfaces. Their macroscopically and microscopically continuous structure differentiates them from striations and suggests they form by ductile processes. These surfaces are commonly decorated by welded, finely comminuted particles [e.g., *Power and Tullis*, 1989; *Kirkpatrick et al.*, 2013]. In some recent experimental studies, development of slickenlines has accompanied strain softening, and it has even been suggested that there is a link between the formation of the shiny surfaces and this mechanical evolution [*Chen et al.*, 2013].

1.2. Morphology of Fault Surfaces

The descriptions of natural slip vector-parallel lineations on an active normal fault, Death Valley, California, presented by *Power et al.* [1987] and *Power and Tullis* [1989], demonstrate typical geometry of these features. These authors determined amplitude over wavelength ratios of 1:100 (rough) to 1:500 (smooth) and noted the presence of grooves, ridges, sheltered gouge tails, and spoon-shaped depressions.

Surface topography of faults can be measured at a range of scales using methods such as light detection and ranging [e.g., *Renard et al.,* 2006], atomic force microscopy (AFM) [e.g., *Chen et al.*, 2013], and white light interferometry (WLI) [e.g., *Renard et al.*, 2012]. From such three-dimensional data sets that cover length scales from nanometer to tens of meters, roughness is quantified using measures such as the root mean square (RMS) of the surface/roughness (the standard deviation of height differences) at a given length scale and the Hurst exponent that describes the scaling property of roughness [e.g., *Pei et al.*, 2005; *Candela et al.*, 2009, 2012; *Renard et al.*, 2012; *Chen et al.*, 2013]. It is observed that fault roughness increases as a power law of length scale on faults [*Sagy et al.*, 2007; *Candela et al.*, 2012] and it has been proposed that it also slightly decreases with slip [*Brodsky et al.,* 2011]. Furthermore, there seems to be a minimum wavelength for slickenlines, ranging from 4 to 500 μm on different fault surfaces, below which dimension plastic yielding prohibits the development of systematic topography [*Candela and Brodsky,* 2016].

The kinematic processes involved in slickenline development were discussed by *Renard et al.* [2012]. These authors described experimentally generated striations in halite, observing that gouge formed on surfaces and that gouge particles spread perpendicular to the slip direction as they were plowed out of the way of the indenter, to generate the slickenlines.

The natural slickenlines described by *Power and Tullis* [1989] have thick accumulations of fine-grained quartz to either side of their surfaces, so we infer a similar lateral transport of comminuted material occurred in that case.

1.3. Microstructure of Materials That Form Slickenlines

The near-surface gouge material surrounding striated or slickenlined fault surfaces in a range of previously described experimental and natural samples displays a few common microstructural characteristics, from which deformation mechanisms have been inferred. Fine, angular fragments of the protolith are inferred to be generated by comminution/wear, which may be stimulated by differential thermal expansion during frictional heating [*Hirose et al.*, 2012]. The materials may have crystallographic preferred orientations (CPO) [e.g., *Smith et al.*, 2011], inferred to result from either alignment of crystallographic axes of inequant fragmented particles, oriented precipitation of crystals in a strain field [e.g., *Power and Tullis*, 1989], attempted minimization of surface energy by grain rotation during sintering [e.g., *Verberne et al.*, 2014; *Toy et al.*, 2015], or crystal plastic processes such as dislocation creep [e.g., *Fondriest et al.*, 2013].

For example, the near-surface gouge material for slickenlines described by *Power and Tullis* [1989] has a range of grain sizes, mostly from 0.01 to 0.1 μm. These grains have high surface energy configurations (e.g., entire grains are included in other grains, very irregular grain boundaries are common) but they are dislocation free. They also contain a CPO that is absent in protolith grains with straight grain boundaries and 120° triple junctions. *Power and Tullis* [1989] infer generation of the small grains by comminution, then oriented growth by

solution-transfer resulted in the CPO but acknowledge dislocation creep, or alignment of inequant comminuted grains by shear could also have occurred.

1.4. Relating Fault Structure and Mechanics

Relationships between slickenline morphology, near-surface gouge material microstructure, and mechanical behavior can be determined from rock deformation experiments. For example, in experiments at room temperature and seismic slip rates on dolomite blocks, angular fragments <10 μm of protolith, ragged pits, and elsewhere, smooth elongate grooves, form on and around the sheared surface [*Chen et al.*, 2013]. In this case, surface morphology measured using AFM and quantified as root-mean-square (RMS) roughness yielded a positive correlation between surface roughness and friction coefficient (also measured by AFM). These authors propose frictional heating to 400°C during slip facilitated plastic behavior allowing the smooth surfaces to develop.

Giger et al. [2008] sheared quartz gouge in presence or absence of water at temperatures from 500°C to 927°C and slip rates of ~ 0.15 μm s^{-1}. They report slickenlines developed on localized slip surfaces within the gouge only in the experiments with water and demonstrate well developed features in their experiments at 800°C that are very similar to those we describe in the present study. All their slickenlined samples also experienced strain softening, but there is no discussion of whether all strain-softening samples developed slickenlines, nor if these features were uniformly absent in slip-hardening samples. Presence or absence of slickenlines at lower temperature or under dry conditions was also not discussed; i.e., they did not systematically consider the conditions that lead to striation development or otherwise.

Hirose et al. [2012] considered the mechanical implications of fault gouge (wear product) development based on experimental shear of sandstone, granite, and diorite at high velocity and room temperature. They observed a power law relationship between friction coefficient, $\mu = \tau/\sigma_n$, and wear rate (the rate of generation of new particles by comminution, defined as thickness of gouge layer/slip) that evolved to an exponential relationship at higher velocities, inferring this occurred as frictional heating and thermal fracturing became important. This exponential increase in wear production rate meant that surface energy became an increasingly important energy sink with increasing velocity. An explicit link to formation of slickenlines was not discussed, but the smoothness of their fault surfaces increased with increasing displacement and slip velocity. We infer from their results that fault smoothing in the direction of slip (i.e., slickenline formation) is a manifestation of processes that lead to slip weakening, which would increase efficiency of continued slip on the fault surface, but that such an increase in efficiency in their experiments was offset by the enhanced wear production rate.

The results of these previous studies inspire us to question whether there is a specific property of the material that makes up slickenlines that facilitates slip weakening (and evolution of the frictional strength versus wear rate relationship)? We address this question in context of our own experimental data sets. Specifically, we have deformed fragments of optically flat silica discs embedded in synthetic gouge under hydrothermal conditions. The initial flatness of the disc fragments provides a reference geometry before deformation. We observe that striations and slickenlines formed on the silica disc fragment surfaces. Herein we consider (1) if there is any relationship between striation morphology, temperature, or shear strain (γ), at constant pressure; (2) what processes and deformation mechanisms accommodated striation or slickenline development under these conditions; and (3) whether causal relationships exist between these processes and the mechanical behavior of the shearing system that might allow us to better understand the rheology of natural faults decorated by striations and slickenlines.

2. Methods

2.1. Experiments

The experiments were performed using the hydrothermal rotary shear apparatus at the HPT laboratory, Utrecht University. Details of the experimental setup are described by *Niemeijer et al.* [2008]. In brief, the apparatus consists of an internally heated pressure vessel located inside an Instron 1362 loading frame. Powdered synthetic gouge samples are sandwiched between two ring-shaped Ni-alloy (René 41) pistons with an outside diameter of 28 mm and an inside diameter of 22 mm. The piston surfaces are grooved with teeth with an average height and spacing of ~0.1 and 0.2 mm, respectively. The synthetic gouge sample is held in
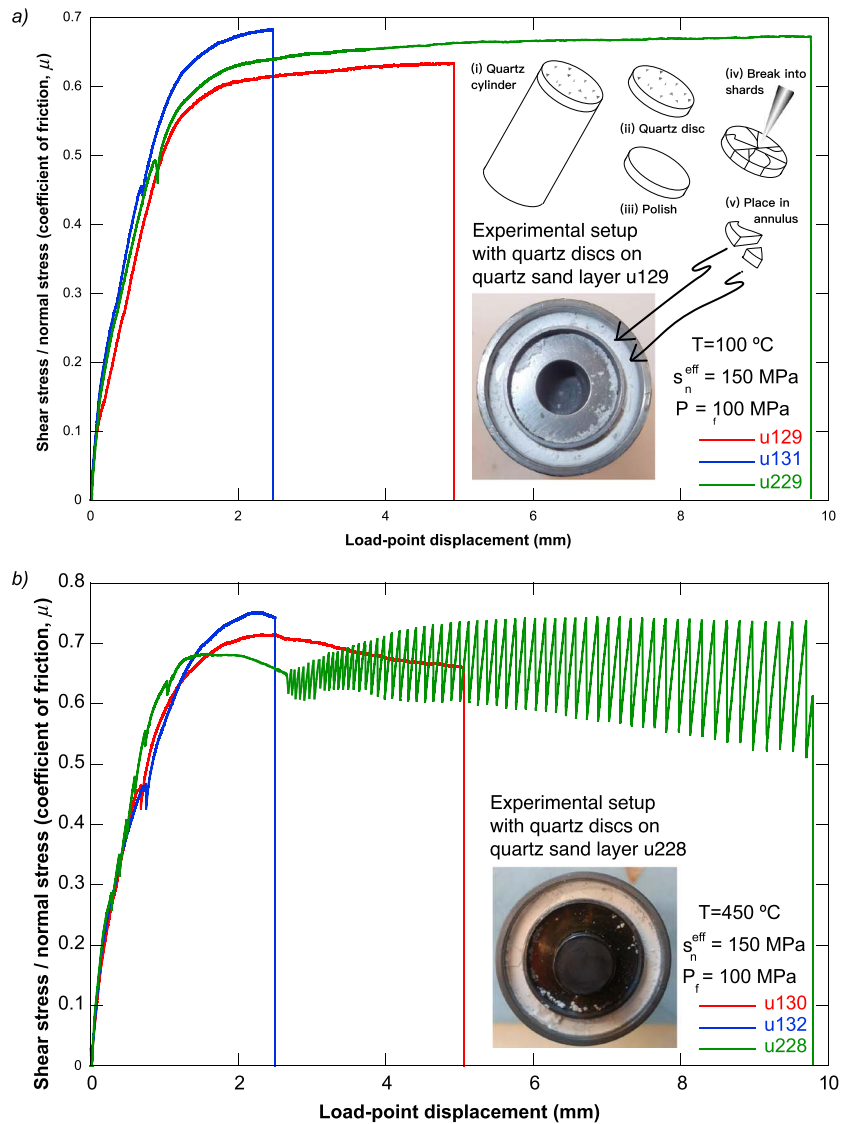
Figure 1. Friction coefficient (μ = shear stress/ normal stress) vs. displacement for experiments to all slip increments performed at (a) 100°C and (b) 450°C. Photographs show top view of experimental apparatus, containing quartz sand and disc fragments. Process to make quartz disc fragments illustrated schematically at top right (i)–(v).

place by two Ni-alloy rings coated with a Molykote spray to reduce friction. Normal load is applied to the sample through an upper fluid pressure-compensated piston head with internal O-ring seals. The pressure vessel is filled with distilled water, which is pressurized using a manual syringe pump. Rotation of the lower piston is achieved using an electromotor geared to the bottom platen through two gearboxes of 1:100 reduction. The upper piston is held stationary through an arm equipped with two load cells, measuring the torque, while the lower piston is rotated at a constant velocity.

Our synthetic gouge material consisted of Sil-CO-Sil® 125 quartz powder (U.S. Silica Company), which comprises subangular to angular grains of SiO_2 with a median grain size of 22 μm. About 0.3 g of quartz powder was deposited on the bottom piston with the confining rings in place and gently tapped. On this surface, we placed several ~0.5 mm thick and typically $<5 \times 10$ mm long/wide slivers of quartz, which are fragments of discs cut from a cylindrical core drilled perpendicular to the long axis of a natural single crystal and mechanically polished using ≤ 1 μm diamond paste. The method of making these is illustrated schematically in Figure 1. The flat side of the disc fragments was placed parallel to the piston surface and therefore parallel to the imposed shear plane. Finally, we deposited another 0.3 g of quartz powder to obtain a

Table 1. List of Experiments and Corresponding Conditions

Experiment	Temperature (°C)	σ_n^{eff} (MPa)	P_f (MPa)	h_{final} (mm)[a]	x (mm)[b]	Shear Strain
u129/ U_VT_003	100	150	100	1.06	4.93	4.54
u130/ U_VT_004	450	150	100	0.61	5.06	7.99
u131/ U_VT_005	100	150	100	1.09	2.47	2.20
u132/ U_VT_006	450	150	100	0.61	2.51	3.94
u228/ U_VT_007	450	150	100	1.16	9.79	8.25
u229/ U_VT_008	100	150	100	1.18	9.76	7.93

[a]Final gouge thickness under normal load.
[b]Displacement.

synthetic gouge layer with a starting thickness of ~1.5 mm. We performed six experiments at a constant applied normal stress of 150 MPa (roughly equal to the effective normal stress), a constant pore fluid pressure of 100 MPa and temperatures of 100°C and 450°C (Table 1). In each experiment, the sample was left to equilibrate at the desired conditions for about 1 h after which we sheared each sample at 1 μm/s for total displacements of x = ~2.5, 5.0, and 9.8 mm (Table 1).

2.2. Sample Treatment and Imaging Techniques

At the end of the experiments, the quartz disc fragments had mostly broken into chips much smaller than the starting material. We were able to find a few of these chips in each sample. These were mounted on carbon tape and carbon coated for examination by secondary electron imaging on an FEI Quanta 3D FEG focused ion beam (FIB)-SEM at GeoForschungsZentrum (GFZ) Potsdam. To investigate deformation mechanisms within the disc fragments, a single transmission electron microscopy (TEM) foil was milled from a quartz disc fragment from experiment u228 (which has the most well-developed and distinctive surface morphology), using a focused ion beam (FIB) technique [e.g., *Wirth*, 2004]. TEM analyses were performed in an FEI G2 F20 X-Twin TEM with a Schottky field emitter as electron source, also operating at GFZ Potsdam. Bright-field and darkfield images were usually acquired as electron filtered images applying a 20 eV window to the zero-loss peak. Electron diffraction patterns were recorded on image plates.

The topography of the surfaces of some of the disc fragments was determined via white light interferometry, WLI (Wyko 2000 Surface Profiler from Veeco) and atomic force microscopy, AFM (Nanowizard®4 AFM from JKP). The horizontal spatial resolution at the highest magnification conditions is about 500 nm for WLI and 12 nm for AFM. The height precision of the WLI when it is used to measure a flat glass surface is <1 nm. The height fields were processed to remove the planar tilt of the surface. The grain size of the gouge recovered at the end of the experiments was also measured. Pieces of deformed samples with a total weight of ~0.25 g (i.e., 40% of the original sample, and all that could be feasibly recovered after the experiments) were gently disaggregated using a pestle and mortar while keeping the sample saturated with ethanol. A Malvern laser particle sizer able to measure grains >30 nm was subsequently used to obtain the particle size distribution.

3. Results

3.1. Mechanical Data

We show friction coefficient ($\mu = \tau/\sigma_{n,\,\text{eff}}$, ignoring cohesion) versus displacement plots of all experiments in Figure 1, where τ is the recorded shear stress, and $\sigma_{n,\,\text{eff}}$ is the effective normal stress. Both normal and shear stress were corrected for the contribution of the internal seals using calibration runs provided in *den Hartog et al.* [2012]. All samples show a quasi elastic linear loading initially, followed by displacement hardening for experiments at 100°C (Figure 1a). For the experiments performed at 450°C (Figure 1b), we observe displacement weakening after a broad peak in friction was reached at around 2 mm of displacement. In all experiments at 450°C, we observed some unstable stick-slip events during the load-up. In addition, regular stick slips that grow in amplitude with ongoing displacement were observed for experiment u228, which was sheared to 9.8 mm. We attribute the small variations in friction observed to variations in starting gouge layer thickness as well as the number, size and thickness of the quartz slivers. The average value of friction corresponds well with previous work using the same material but slightly different conditions [*Niemeijer et al.*, 2008] as well as other works on quartz sand [e.g., *Chester and Higgs*, 1992]. The occurrence of stick
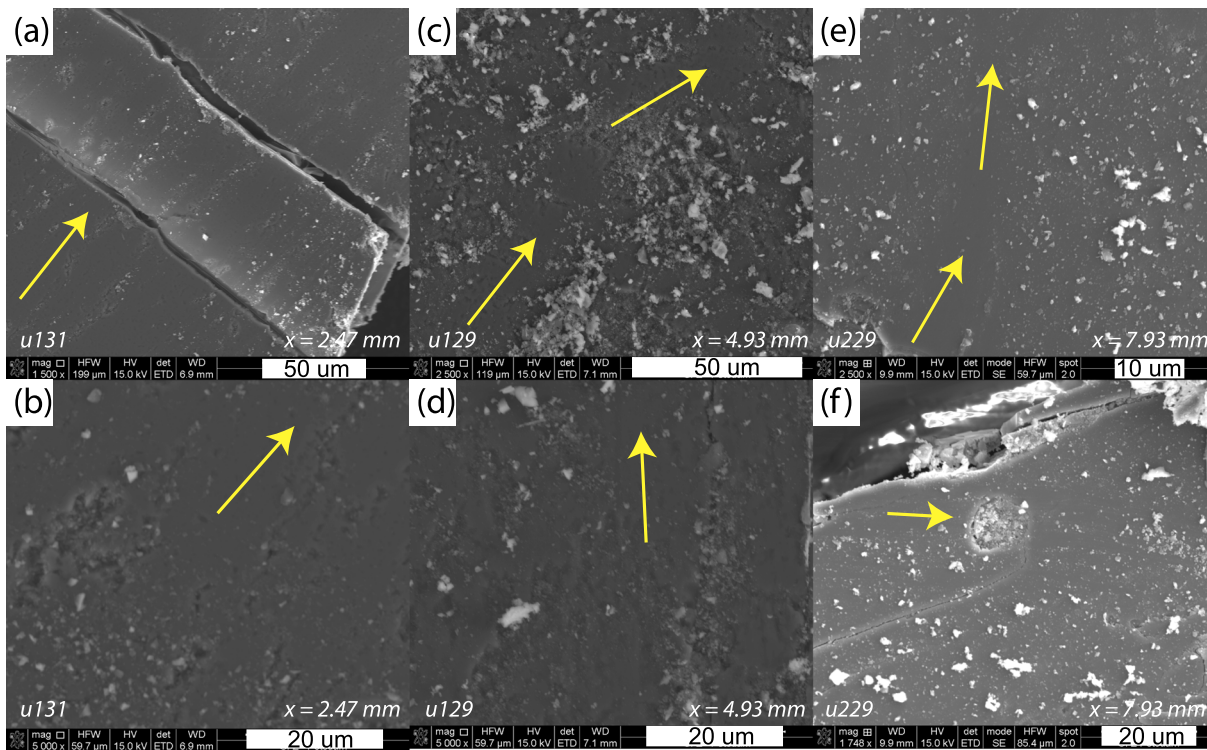
Figure 2. Scanning electron microscopy (SEM) images showing representative surface decoration and topography of disc fragments sheared at 100°C to a range of total displacements (labelled "*x* =" in lower right of each image). Experiment numbers are labelled at lower left. The top row is low magnification and the lower row is higher magnification. Note in particular discontinuous and sublinear trails of gouge on all surfaces and indented regions decorated by angular quartz particles (<5 μm)—these have linear shapes in (b) and (d) but are subrounded pits in (f). In each case a yellow arrow parallels the inferred slip direction. In (c) and (e) two arrows demonstrate changes in this orientation across the imaged area.

slips in experiment u228 is most likely the result of a lower fault surrounding stiffness due to the fact that the simulated gouge in this experiment was up to 40% thicker than in the other two experiments at 450°C. Assuming that the rate-and-state frictional parameters *(a-b)* and d_c are the same in all experiments, the stability criterion is fulfilled for a lower stiffness [*Scholz*, 1998]. Unstable stick slips were also observed in past experiments on quartz gouges at 450°C, 100 MPa effective normal stress, 200 MPa pore fluid pressure and 1 μm s^{-1} [*Niemeijer et al.*, 2008, Figure 9].

3.2. SEM and WLI Observations

Newly generated gouge, comprising angular particles of quartz (presumably comminuted pieces of the starting materials, i.e., quartz powder and quartz disc fragments), is present on the surface of all quartz disc fragments (Figures 2 and 3). In places it is distributed in linear trails (Figure 2a). In a few cases the trend of these trails changes slightly along their length (Figures 2c and 2e). The surfaces of all disc fragments contain depressions with linear (Figures 2d, 2e, 3b–3d, 3h, 3i, 4d, and 4e), elliptical (Figure 2f), or scalloped shapes (Figures 3e and 3f). Additionally, smooth grooves, with wavelength <10 μm and amplitude <0.7 μm (Figure 4), decorate all the samples deformed at 450°C (Figure 3), but none of the samples deformed at 100°C. These smooth grooves are best developed at highest displacement (experiment u228 and Figures 3g–3i), particularly on steps in the quartz disc fragment surfaces (Figure 3i). In the lowest displacement, higher temperature experiment (u132 and Figures 3a–3c and 4d), the grooves have shorter wavelength, more angular cross-sectional morphology, and delineate two trends on the disc fragment surfaces.

In the disc fragments deformed at 100°C the depressions only contain angular particles of a range of diameters ≤5 μm (Figure 2f). Conversely, in the disc fragments deformed at 450°C, the depressions contain both angular particles and scattered rounded beads mostly ~200 nm in diameter. These beads are especially well developed in the highest displacement experiment at this temperature (u228 and Table 1 and
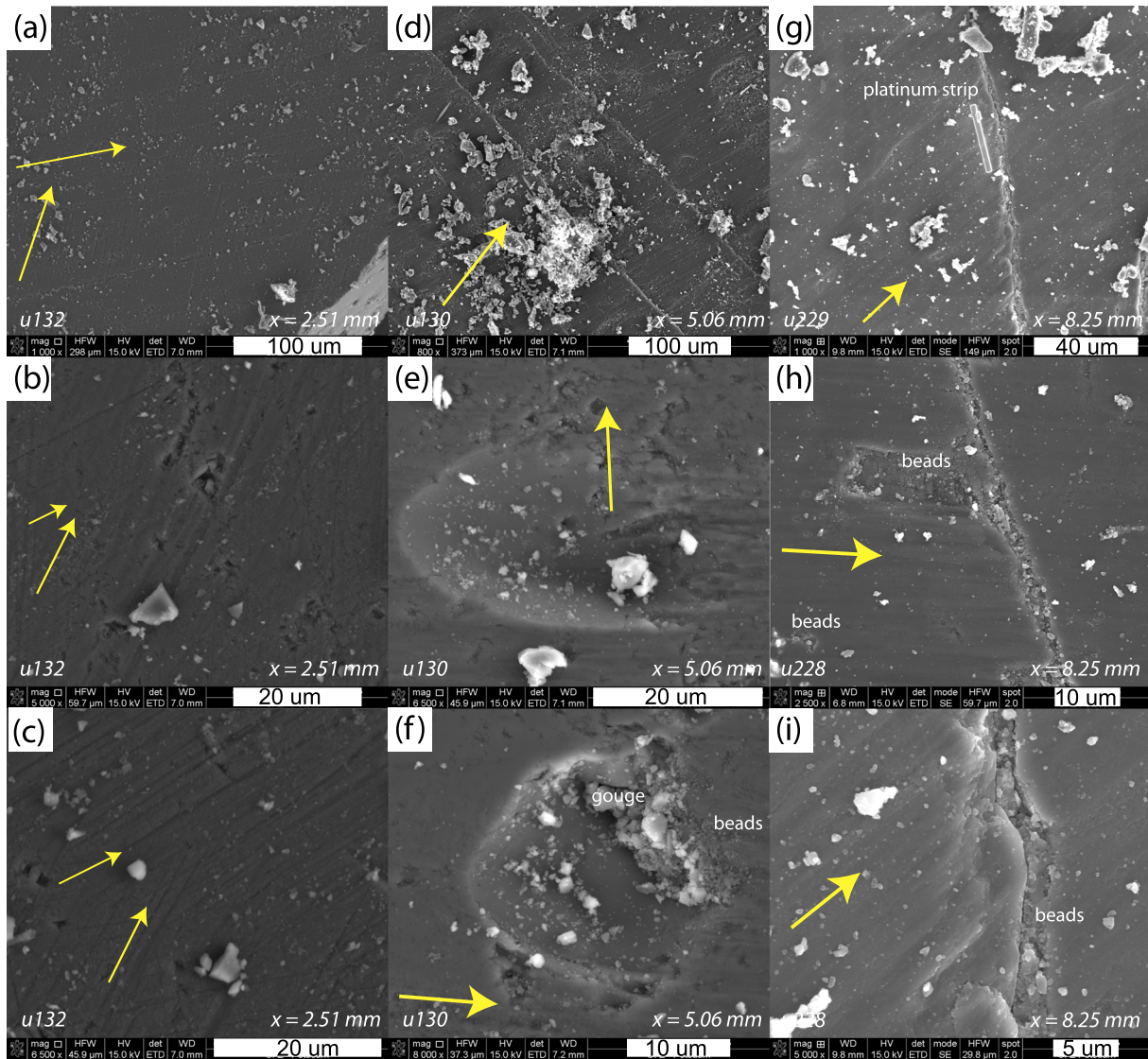
Figure 3. SEM images showing representative surface decoration and topography of disc fragments sheared at 450°C to a range of total displacements (labelled "x =" in lower right of each image). Experiment numbers are labelled at lower left. Image magnification increases down the page. Note in particular less well-developed slickenlines with two slip directions in the lowest displacement experiments (a), (b), and (c); spoon-shaped pits in (e) and (f) decorated by angular shards with a range of grain sizes (inferred gouge as labelled). Adjacent to the pit in (f) there are also subrounded particles (inferred beads as labelled). The most rounded beads are observed in the highest slip experiment, where they are smaller than gouge (g), and decorate both grooves (h), and steps in the disc fragment surfaces (i). FIB foil illustrated in Figure 6 was extracted parallel to the platinum strip labelled in (g). In each case yellow arrow parallels the inferred slip direction(s).

Figures 3g–3i) but are present in all samples. They are abundant in all depressions within this sample, including slip-perpendicular steps within the sample surface (Figure 3i). They are slightly elongated with a preferred long axis orientation perpendicular to the linear grooves (Figures 5a and 5b) and sometimes seem to be sutured into strings also aligned perpendicular to the grooves. The beads have a relatively regular dimension (~200 nm in diameter—Figure 5c) but a few smaller beads with undulating surfaces may reach dimensions of tens of nm.

3.3. TEM Observations

In order to investigate the microstructure of the near-surface gouge material and the rounded quartz beads, a TEM foil was cut from a quartz sliver of experiment u228, which was deformed at 450°C and to 9.8 mm displacement, perpendicular to the disc fragment surface and inferred slip direction (Figure 6a). In this foil we were able to make observations of a cross section of the undulating surface, the beads, and the near-surface
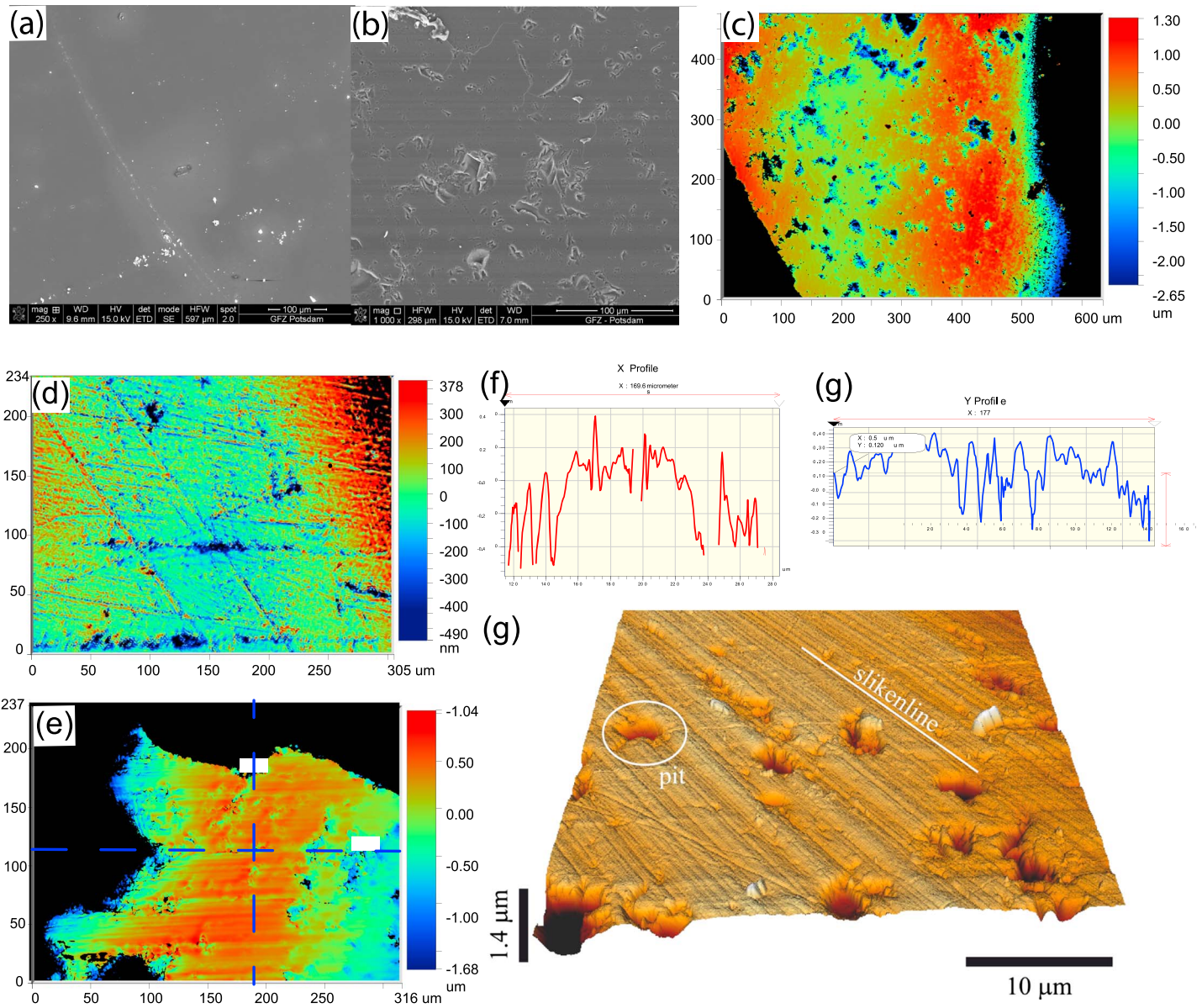
Figure 4. (a)–(c) Representative surface decoration and topography of starting material for experiments illustrated in SEM images for (a) ~9.8 mm displacement experiments, and (b) ~2.5 and ~5 mm displacement experiments. The faint horizontal bands in (b) are a charging effect, not topographic variations on the sample surface. (c) Elevation map of surface of the latter material via white light interferometry. White light interferometry elevation maps are also presented for surfaces of (d) u129, $T = 100°C$, $x = 4.93$ mm, and (e) u132, $T = 450°C$, $x = 2.51$ mm. The topographic profiles illustrated in (f) and (g) are derived from transects parallel and perpendicular to the slickenlines developed in u132 at locations demonstrated by dashed blue lines in (e). (g) illustrates a three-dimensional rendering of sample u228, based on atomic force microscopy.

gouge material. These reveal that there are no significant systematic dislocation arrays in the near-surface gouge material, although a few sporadic arrays are observed (Figure 6b). One distinct set of microfractures form an anastomosing array parallel to the disc fragment surface (Figure 6c), and sporadic fractures are observed elsewhere (Figure 6d). There are also a few linear fluid inclusion trains (Figure 6e, arrowed).

Careful observation of the foil at a range of tilt angles within the TEM confirmed that, like most of the near-surface gouge material, the silica beads do not contain dislocations. Electron dispersive spectroscopy (EDS) confirms they are composed of Si and O (Figures 6e and 9b–9d). Moiré patterns within some of these beads (Figure 6f) demonstrate that they are crystalline. Conversely, amorphous silica that never shows Moiré patterns fills the space between the rounded quartz beads (Figures 6d–6f) but does not form a film outside the beads at the surface.
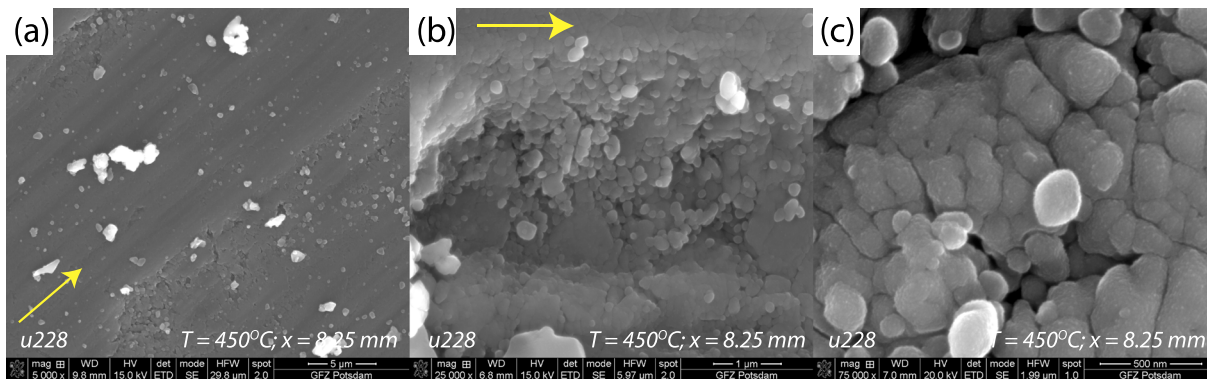
Figure 5. SEM images of u228 (T = 450°C, x = 9.8 mm) demonstrating morphology of silica beads. Magnification progressively increases from (a) to (c). Yellow arrows are parallel to inferred slip direction.

3.4. High-Resolution Surface Topography Data

From topography data of the silica disc fragment surfaces measured by atomic force microscopy and white light interferometry (Figures 4c–4g and insets in Figure 7), the slickenlines could be identified for the samples deformed at 450°C. In a profile perpendicular to the slickenlines (e.g., Figure 4g), the grooves show spatial wavelengths <10 μm and height amplitudes <0.7 μm (Figures 4f and 4g). The evolution of roughness with spatial scale was calculated by performing one-dimensional Fourier transforms of the topography data, following the procedure described in *Candela et al.* [2009]. The scaling exponents H were calculated for the segments of the Fourier transforms that show a linear trend in a log-log plot (Figure 7). Results show that H is constant for samples deformed at 100°C (Figure 7, red curve), whereas it changes at a characteristic cross-over length scale L^* = 3–5 μm, which is the minimum wavelength of the slickenlines, for the samples deformed at 450°C. Above L^*, the surface is very flat (H = 0.1 ± 0.05), which corresponds to the initial planar disc fragment surfaces; below L^*, it shows a value of H = 0.5 ± 0.1, typical of fault roughness [*Candela et al.*, 2009]. Another characteristic crossover length scale is observed below 0.1 μm on the atomic force microscopy data (magenta curve in Figure 7), below which the disc fragment surface is flat and which could correspond to the plastic flattening of asperities at small scale.

3.5. Grain Size Data

The grain size distributions of the gouge material at the end of the experiments (Figure 8) are similar for all samples, with medians around 20 μm, similar to the 22 μm median grain size of the starting synthetic gouge. This indicates that grain size reduction within the gouge was minimal during the experiments. The two samples sheared to highest strains at low temperatures (u131 and u229) have broader distributions of grain sizes with more grains in the smaller particle size range. Most samples, particularly u132 and u229, have a significant population of grains >100 μm. We infer these were clusters of many finer particles that were welded together during shear and not completely disaggregated on removal from the apparatus.

4. Discussion

4.1. Interpretation and Classification of the Linear Features

The microstructural observations allow interpretation of the relative importance of deformation mechanisms such as brittle failure of the near-surface gouge material, surface wear by comminution, deformation of the near-surface gouge material by crystal plasticity, and solution transfer of material. We consider that linear trails of gouge, scratches, and grooves on the quartz disc fragment surfaces (Figures 2, 3a–3c, and 3g–3i) are parallel to the relative displacement of the quartz disc fragments with respect to the surrounding gouge particles during shear. The scratches that are weakly developed in the low temperature experiments (u129 and u131 and Figure 2) and well developed at low displacement increments in the higher temperature experiments (u132 and Figures 3b and 3c) are most appropriately called striations, while the smooth grooves that are most well developed in the higher displacement, higher temperature experiments (e.g., u228 and Figures 3g–3i and 5a) are slickenlines according to the definitions presented earlier.
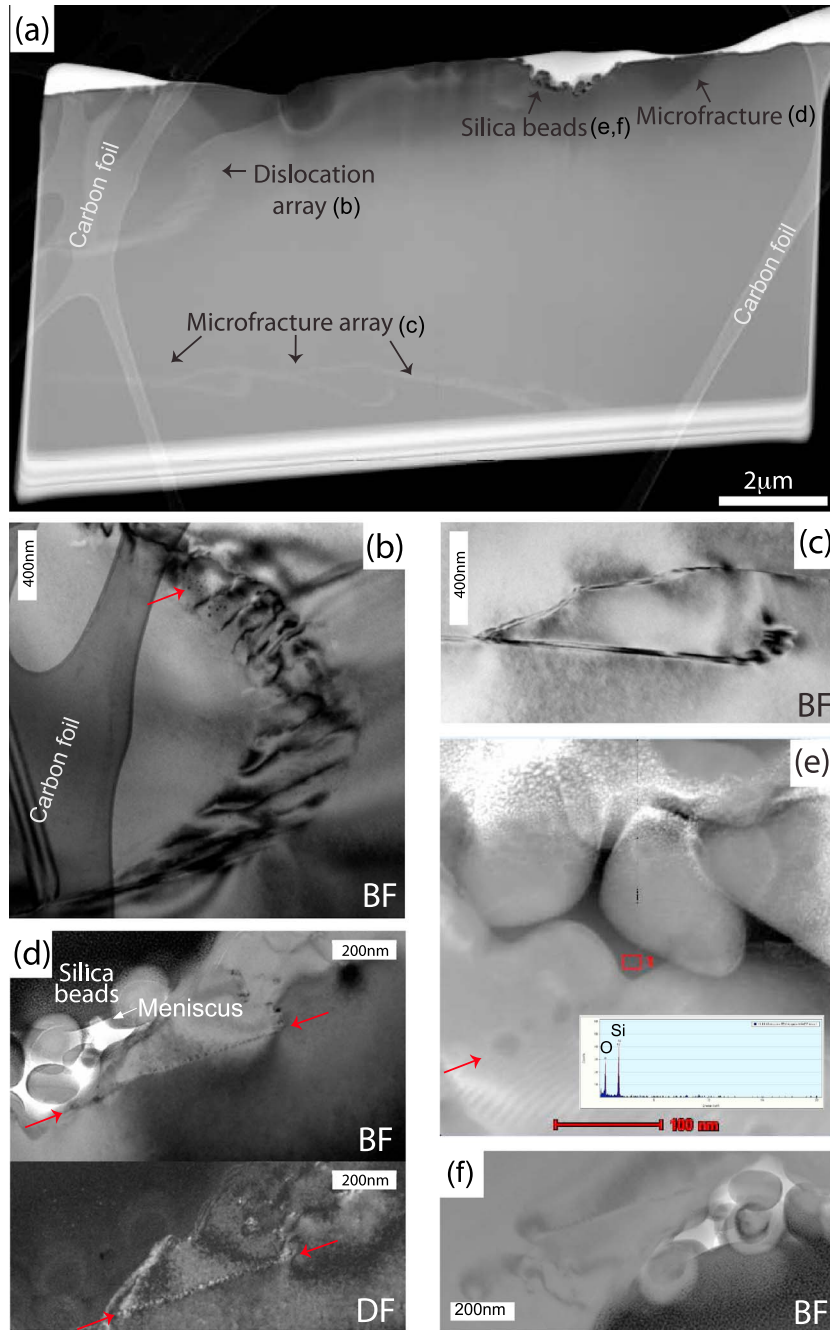
Figure 6. TEM images from u228, $T = 450°C$, $x = 9.79$ mm. (a) High-angle annular darkfield (HAADF) image overview of foil. Bright material is platinum that was deposited on top of the sample prior to FIB milling. The top surface of the foil is the grooved surface of the quartz chip. Unlabelled bright patches are related to the underlying perforated carbon foil. TEM bright-field (BF) and darkfield (DF) images showing (b) an array of dislocations and solid inclusions (arrowed); (c) diffraction contrasts within anastomosing planar microfractures. Variations in width of the diffraction contrast reflects change in the dip of the microfracture with respect to the sample surface; (d) a microfracture (between red arrows) adjacent to silica beads with an interstitial meniscus. (e) HAADF image of enlarged view of silica beads (at top of image), and fluid inclusions in healed microfracture (arrowed). Inset shows EDS spectrum from amorphous silica interstitial to beads (See also Figures 9b–9d). (f) TEM bright-field image demonstrating an example of Moiré patterns in the beads, which demonstrates their crystalline state. Conversely, the material surrounding the beads never shows diffraction contrast, proving that it has an amorphous state.
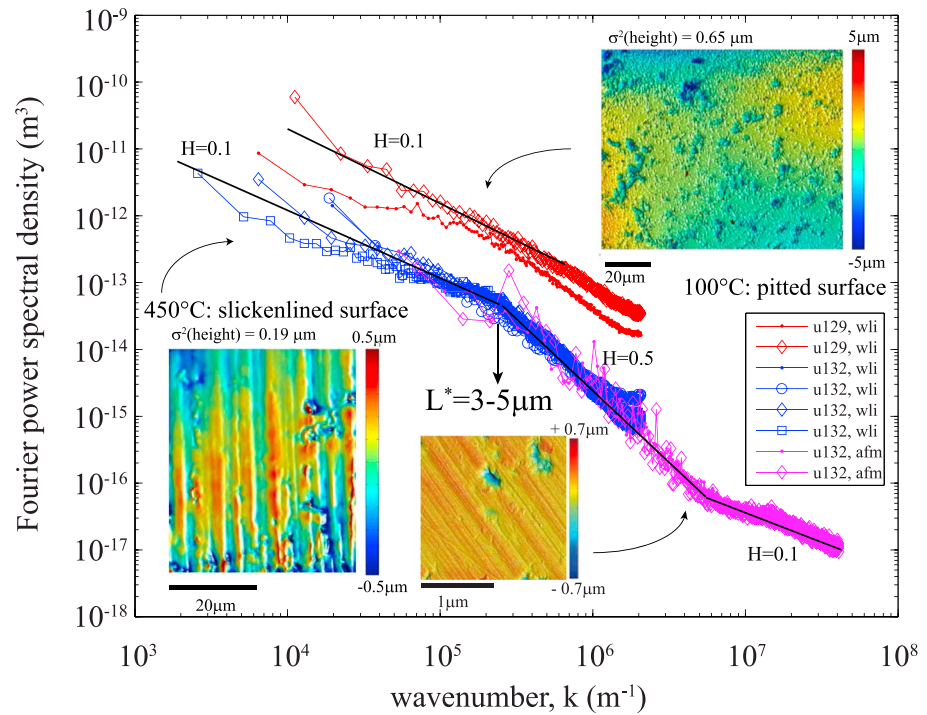
Figure 7. Topography data gathered by atomic force microscopy (AFM) and white light interferometry (WLI). The spectra were measured on profiles perpendicular to the grooves on slickenlined surfaces. Inset images demonstrate surface topography of (a) u129, $T = 100°C$, $x = 4.93$ mm, and (b and c) u132, $T = 450 °C$, $x = 2.51$ mm at different magnifications. The plot (d) demonstrates a numerical measure of the surface roughness. "H" are Hurst roughness exponents, calculated as outlined in the text (equation (1)). $L*$ is the length scale or wavelength of the slickenlines.

We infer the linear trails of fluid inclusions (Figure 6e) are a section through a planar array of inclusions and that these are similar to planar deformation features of *Blenkinsop* [2000], which are healed microfractures. Along with the sporadic unhealed microfractures, these features demonstrate that some permanent defor- mation of the near-surface material was accomplished by brittle fracture, i.e., stress corrosion cracking [*Atkinson and Meredith*, 1981; however, we cannot guarantee this occurred during the experiment rather than during sample preparation. Conversely, the general absence of dislocations suggests that dislocation glide was not a significant strain-accommodating mechanism at any stage.

The angular particles with variable size observed within pits in the low temperature samples (Figure 2f) are most likely to be brittle wear products or "gouges" formed by comminution of both the sample surface and the quartz sand. These microstructures were probably developed when the brittle yield strength of these materials was exceeded at contact points between quartz sand particles and the surfaces of quartz disc fragments. These impacts also resulted in formation of the striations and pits. At lower temperatures, rounded pits, or scratches that only extend across part of the disc fragment surface are prevalent, so impacts between particles and disc fragment surfaces must have been short lived. Ongoing shear under these conditions must have involved mostly granular flow and cataclasis of angular quartz particles with limited interactions between the particles and the disc fragment surface, due to the small surface area of contact points and short contact times.

At higher temperatures, the rare scallop-shaped pits are probably initial impact sites that have been flattened and rounded by a pressure solution creep mechanism. We infer that, as at low temperature, some comminu- tion accompanied initial impact and pit formation. However, particularly at large displacements, the slicken- lines delineate parallel arrays that extend across the entire disc fragment surface, indicating particle and disc fragment surface interactions were quite different than at lower temperatures. The most significant implication of the presence of these slickenlines is that the contacts of quartz particles with the disc fragment surfaces were longer lived and affected a greater area at high than at low temperature. This is likely to reflect contact area growth due to either plastic deformation or solution-transfer processes. This must have been a transient
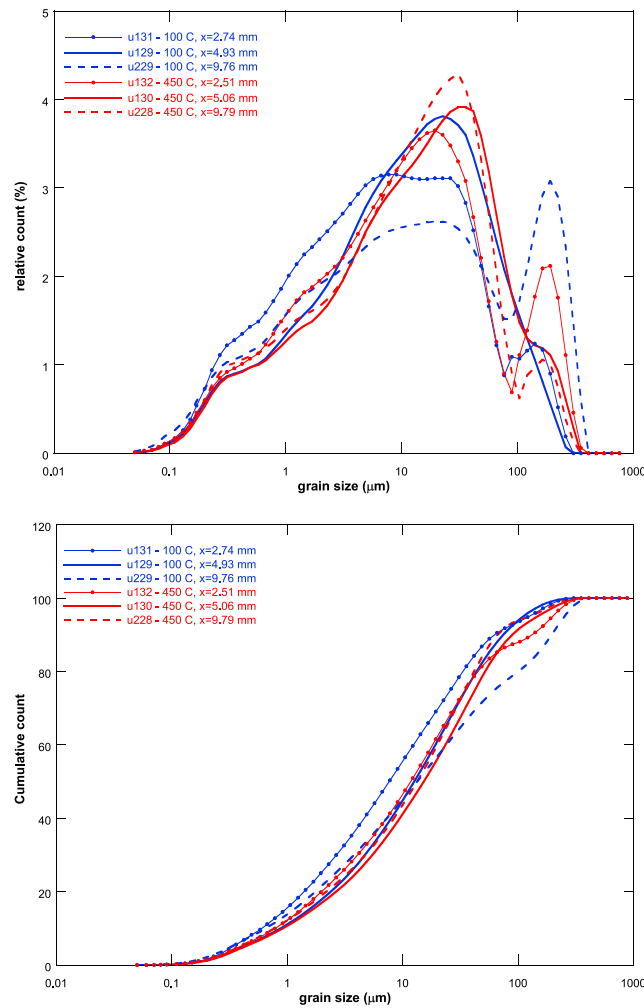
Figure 8. Grain size distributions of simulated gouges recovered from the shear apparatus at the end of the experiments.

process during the early parts of the experiments, because if it had post-dated yielding we might expect both an overall increase in grain size in the higher temperature experimental products, and strain hardening, neither of which are observed (Figures 1 and 8).

If contact growth was by plastic deformation, we would expect dislocations to be generated around the impact structures on the disc fragments, but these are not observed in the TEM foil, so we favor pressure solution creep enhanced dissolution-precipitation as the process for contact area growth. Hydrostatic experiments at P_{conf} = 300 MPa and 480°C have recently demonstrated that silica beads <100 nm diameter with identical appearance to those we observe form by solution-precipitation (A. R. Niemeijer, personal communication, 2017).

Other aspects of our results also point toward the occurrence of pressure solution creep and solution-transfer during the experiments. The amorphous silica deposited between the beads has the morphology of a liquid meniscus, which is consistent with precipitation from a fluid. The high-resolution topography data (Figure 7) are consistent with a pressure solution mechanism for slickenline formation, as explained in the following; the experiments were performed at 150 MPa, far from the plastic limit of quartz whose yield strength at 450°C falls in the range 2.8–4.5 GPa [*Blacic and Christie*, 1984; *Spray*, 1992]. Using the elastic theory of contact of *Hertz* [1881], we can calculate the elastic flattening of single asperities at the silica disc fragment surface, depending on their height, using the same procedure as in *Candela and Brodsky* [2016] [a more detailed description of the methodology can be found in supporting information Part S2; *Blacic and Christie*, 1984; *Bush et al.*, 1975; *Candela and Brodsky*, 2016; *Greenwood and Williamson*, 1966; *Hertz*, 1881; *Hyun et al.*, 2004; *Johnson*, 1985; *Mikic and Roca*, 1974; *Spray*, 1992]. For the observed slickenline wavelength *L** with a normal stress in the range 150 MPa (the normal load imposed by the rig) to 1.5GPa (to account for possible local stress concentrations), elastic flattening of the asperities can be estimated in the range 10^{-7} to 10^{-8} m, a factor 7 to 70 times smaller than the actual height of the slickenlines measured, which is close to 0.7 μm. These calculations also show that the plastic limit is not reached in the disc fragments below the slickenlines, consistent with the absence of dislocations. As a consequence, because the striations and slickenlines do not result from plastic deformation and were not elastically flattened during shear, the argument that they formed by a pressure solution mechanism is strengthened. Note for wavelengths larger than *L**, the surface appears quite flat, and we interpret this effect is due to the fact that the total amount of slip was not large enough to erase the initial flatness of the quartz discs.

Alternative mechanisms for formation of the amorphous silica are by tribochemical reactions, amorphisation due to pressure, and frictional melting [e.g., *Han et al.*, 2011; *Kirkpatrick et al.*, 2013; *Pec et al.*, 2012; *Sibson and Toy*, 2006]. We cannot discard tribochemical reactions, but since calculated asperity pressures are insufficient

to cause plasticity they are definitely too low to stimulate amorphisation. Furthermore, the temperature rise likely on the fault surfaces at these strain rates [cf. *Mitchell et al.*, 2016; *Pec et al.*, 2012] would be less than tens of degrees, insufficient to stimulate melting of crystalline quartz [*Spray*, 1992].

4.2. Origin of Silica Beads

The silica beads could have formed by two processes: either (1) they originated as comminuted gouge fragments that were rounded by surface energy-driven dissolution that minimized local curvature or (2) they precipitated from the fluid. The gouge fragments show a range of sizes <5 μm. We argue against the first origin because, at the constant conditions and fluid chemistry of the experiments, dissolution should occur at a constant rate, so similar thicknesses of all particles should be dissolved. This would result in rounded beads with a range of sizes. Instead, we observe that the beads are mostly 200 nm in diameter.

We estimate the time scale of precipitation (i.e., growth) of silica particles in the shear experiments using existing quartz dissolution/precipitation rate data. The rate of quartz dissolution/precipitation can be described by the reaction $H_4SiO_{4(aqueous)} \leftrightarrow SiO_{2(solid)} + 2H_2O$:

$$V = k.V_q.\left(1 - \frac{Q}{K}\right) \tag{1}$$

where V is the velocity of dissolution/precipitation in m s^{-1}; k is the quartz dissolution or precipitation rate constant (mol m^{-2} s^{-1}); V_q is molar volume of quartz (22.688×10^{-6} m^3 mol^{-1}); K is the equilibrium constant of quartz dissolution at T and P, equal here to the solubility of quartz (mol m^{-3}); Q is the concentration of quartz in the solution (mol m^{-3}).

We define a saturation index, $S = Q/K$. If $S > 1$, precipitation occurs. If $S = 1$, the system is at equilibrium. If $0 < S < 1$ dissolution occurs. K depends on temperature and pressure. The temperature dependence [*Rimstidt and Barnes*, 1980] is

$$\log K_o = 1.174 - 2.028 \times 10^{-3} \times T - \frac{4.158}{T} \tag{2}$$

where K_0 is the quartz equilibrium constant at atmospheric pressure P_0 and temperature T (°K). The pressure dependence is

$$K = K_0 e^{\frac{(P-P_0) \times V_q}{RT}} \tag{3}$$

where P is the pressure (Pa), P_0 is the atmospheric pressure (10^5 Pa), and R is the gas constant (8.32 J/mol/K). The rate constant for dissolution or precipitation, k, which depends on salinity and pH [see *Dove*, 1994], is shown in Figure S1 (supporting information Part S1).

For a given particle the time of precipitation t (s), as a function of the particle radius r (m), is

$$t = \frac{r}{V} \tag{4}$$

The following assumptions are made. (i) The rate of dissolution is equal to the rate of precipitation. This is reasonable when the system is close to equilibrium. Nucleation is not included in this model and we assume that nanoparticles would preexist (10 nm size) and then grow using this rate law. (ii) For $S > 1$, the fluid must be supersaturated with respect to silica, i.e., $Q > K$ in equation (1). (iii) We assume that pressure solution drives the process: so quartz solubility is larger at asperities/grain contacts due to higher stress and lower in pores. Because quartz solubility depends on pressure (σ_n at the contacts and P_f in pores), the difference of quartz solubility between a pressure equal to σ_n and a pressure equal to P_f is chosen as the driving force for precipitation, and the term $(P - P_0)$ in equation (3) is replaced by $(\sigma_n - P_f)$. (iv) The rate of silica precipitation used here is the same for quartz or amorphous silica. (v) The quartz solubility (K) and kinetics constants (k) given by *Rimstidt and Barnes* [1980] and *Dove* [1994] are valid between room temperature and 300°C. We have extrapolated them to 450°C.

The rates of precipitation as a function of particle size at 100°C and 450°C are shown in Figure 9, as well as the time scale for the precipitation of a 200 nm quartz particle as a function of temperature. If dissolution is driven by the overall normal stresses imposed by the apparatus, we find that 200 nm diameter silica beads could have precipitated from the solution used in the experiments, at the experimental confining and fluid pressures, in ~250 s at 450°C, well within the time frame of the experiments. Conversely, at 100°C,

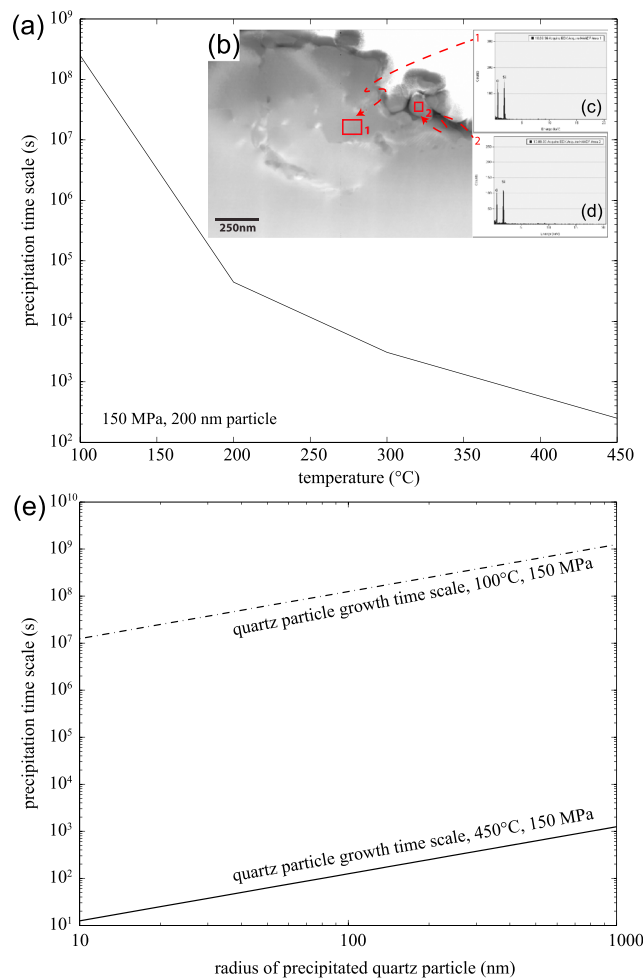**Figure 9.** Estimation of the rate of quartz beads precipitation in the experiments. (a) Time scale for the precipitation of quartz beads at the experimental conditions (450°C, 150 MPa differential stress). Inset: EDS spectra captured using TEM. (b) Bright-field field image of foil; location shown in Figure 6e. Spectra are derived from (c) quartz disc fragment (spectrum 1) and (d) silica beads (spectrum 2). Both only contain peaks for oxygen and silicon. (e) Calculated time for precipitation of silica particles of various dimensions at the two experimental temperatures, 100°C and 450°C.

precipitation would take ~2.5×10^8 s (i.e., ~8 years). Overall, during the experiments the samples were maintained at elevated temperatures for a little over 3 h. In this time, our calculations suggest silica beads up to 500 nm could form at 450°C, which is in the same order of magnitude as the 200 nm beads observed in the experiments.

4.3. Kinematic Considerations

Curved gouge trails in low temperature experiments (Figures 2c and 2e) and multiple crosscutting slickenlines (Figures 3a–3c) are evidence of rotation of quartz slivers within the shearing gouge. At higher temperature this evidence is only apparent in the low displacement experiments. Slip vectors inferred for samples with well-developed shiny slickenlines composed of sintered silica beads maintain one orientation across the entire disc fragment surface. This suggests that once these slickenlines develop, slip parallel to them becomes particularly mechanically favored. Conversely, formation of scratches does not influence disc fragment/gouge kinematics.

4.4. Mechanical Consequences of Slickenline Formation

It has previously been suggested that generation of amorphous silica on fault planes [*Di Toro et al.*, 2004], as well as smoothing of the fault surface in the direction of slip [*Chen et al.*, 2013], results in strain softening and facilitates ongoing shear [*Di Toro et al.*, 2004; *Hirose et al.*, 2012; *Chen et al.*, 2013]. It is also mechanically unfavorable to change slip direction once a surface anisotropy such as the observed slickenlines has developed, because this requires additional wear [*Power et al.*, 1987]. Our observations further indicate that formation of crystalline material from an amorphous phase, followed by suturing of these crystals in a systematic arrangement, also facilitates slip. Our mechanical data demonstrate that strain softening occurs only in the higher temperature samples. However, we note that the experimental apparatus measures the bulk behavior of the quartz sand with embedded quartz disc fragments. Sand-disc fragment surface interactions are only a minor component of the system, and so they might not dominate the bulk behavior. Nevertheless, we believe the microstructural observations are sufficient proof that slickenline formation facilitates strain softening.

This effect can only be significant in the Earth's crust at temperatures where crystal growth will occur during a slip event. This is only realistic for typical earthquake rise times of tens of seconds [*Sibson*, 1989] for temperatures in excess of 450°C—where creep mechanisms typically dominate [*Scholz*, 1998]. However, for shear zones slipping at rates similar to those of our experiments, we expect this mechanism to be effective at

greenschist facies conditions. In addition, in this study we did not consider the possible effects of variation in slip rate or effective normal stress. These influences should be carefully considered in future work.

Finally, slickenlines composed of welded (partly-)amorphous silica beads similar to those we observe in 450°C experiments have recently been reported on a few natural faults that are thought to have slipped seismically. *Kirkpatrick et al.* [2013] described an amorphous material on the striated surface of the Corona Heights Fault, CA, CA. In TEM they observed rounded cores of crystalline silica embedded in amorphous silica. Similarly, *Kuo et al.* [2016] reported that smooth, polished surfaces on natural faults (fault mirrors) are composed of aggregates of ~1 µm platy silica grains (their Figures 2b–2d). The similarity of these natural rocks to those produced in our experiments leads us to infer all may have formed by similar mechanisms. It is important that shear in our experiments was at subseismic rates; thus, we cannot infer slickenline generation on the natural faults required slip at seismic rates.

5. Conclusions

From our experimental study of the interactions between particles and surfaces sheared under hydrothermal conditions at 100°C and 450°C, at subseismic rates to a range of total displacements, we reach the following conclusions:

1. Slickenlines in quartz only develop at elevated temperature under hydrothermal conditions. These temperatures are sufficiently high for crystalline particles to be precipitated on fault surfaces during shear and to allow time-dependent contact growth to enhance interactions between gouge particles and the disc fragments.
2. The main deformation mechanisms that accommodated slickenline formation were brittle wear and pressure solution-transfer. The latter is most important at elevated temperatures.
3. Microstructural observations suggest that development of slickenlines comprising sintered silica beads in an amorphous silica matrix facilitated strain softening.
4. This strain softening accompanied development of undulations perpendicular to the slip vector, smoothing of the fault surface parallel to the slip vector, and maintenance of a constant slip direction.

The implications of this final conclusion are particularly novel and interesting for interpretation of natural examples. Many natural fault systems do contain a single orientation of striation, slickenfibre, or slickenline. Notable exceptions include slickenfibres within the Chrystalls Beach mélange, New Zealand [*Fagereng et al.*, 2011] and the serpentinite-rich fault system at the base of the Bay of Islands ophiolite, Newfoundland [*Wojtal*, 2001]. In the past, formation of multiple orientations of slickenlines was attributed to kinematically influenced rotation of blocks comprising these shearing systems [cf. *Twiss et al.*, 1991]. However, we suggest that the presence of a multitude of slickenfibre orientations may merely indicate that ongoing shear in these systems was not strain softening, so slip did not occur in a constant direction.

References

Atkinson, B. K., and P. G. Meredith (1981), Stress corrosion cracking of quartz: A note on chemical environment, *Tectonophysics*, *77*(1), T1–T11, doi:10.1016/0040-1951(81)90157-8.

Blacic, J. D., and J. M. Christie (1984), Plasticity and hydrolytic weakening of quartz single crystals, *J. Geophys. Res.*, *89*(B6), 4223–4239.

Blenkinsop, T. (2000), *Deformation Microstructures and Mechanisms in Minerals and Rocks*, 100 p., Kluwer Acad., Dordrecht, Netherlands.

Brodsky, E., J. Gilchrist, A. Sagy, and C. Collettini (2011), Faults smooth gradually as a function of slip, *Earth Planet. Sci. Lett.*, *302*(1–2), 185–193.

Bush, A. W., R. D. Gibson, and T. R. Thomas (1975), The elastic contact of a rough surface, *Wear*, *35*(1), 87–111.

Candela, T., and E. E. Brodsky (2016), The minimum scale of grooving on faults, *Geology*, *44*(8), 603–606, doi:10.1130/G3934.1.

Chen, X., A. S. Madden, B. R. Bickmore, and Z. Reches (2013), Dynamic weakening by nanoscale smoothing during high-velocity fault slip, *Geology*, *41*(7), 739–742.

Candela, T., F. Renard, M. Bouchon, D. Marsan, J. Schmittbuhl, and C. Voisin (2009), Characterization of fault roughness at various scales: Implications of three-dimensional high resolution topography measurements, *Pure Appl. Geophys.*, *166*, 1817, doi:10.1007/s00024-009-0521-2.

Candela, T., F. Renard, Y. Klinger, K. Mair, J. Schmittbuhl, and E. E. Brodsky (2012), Roughness of fault surfaces over nine decades of length scales, *J. Geophys. Res.*, *117*, B08409, doi:10.1029/2011JB009041.

Chester, F. M., and N. G. Higgs (1992), Multimechanism friction constitutive model for ultrafine quartz gouge at hypocentral conditions, *J. Geophys. Res.*, *97*, 1859–1870.

den Hartog, S. A. M., A. R. Niemeijer, and C. J. Spiers (2012), New constraints on megathrust slip stability under subduction zone P–T conditions, *Earth Planet. Sci. Lett.*, *353-354*, 240–252, doi:10.1016/j.epsl.2012.08.022.

de Ronde, C. E. J., R. H. Sibson, C. J. Cray, and K. Faure (2001), Fluid chemistry of veining associated with an ancient microearthquake swarm, Benmore Dam, New Zealand, *Geol. Soc. Am. Bull.*, *113*(8), 1010–1024.

Di Toro, G., D. L. Goldsby, and T. E. Tullis (2004), Friction falls towards zero in quartz rock as slip velocity approaches seismic rates, *Nature*, *427*(6973), 436–439.

Dove, P. M. (1994), The dissolution kinetics of quartz in sodium chloride solutions at 25° to 300°C, *Am. J. Sci.*, *294*, 665–712.

Doblas, M. (1998), Slickenside kinematic indicators, *Tectonophysics*, *295*(1), 187–197.

Engelder, J. T., and C. Scholz (1976), The role of asperity indentation and ploughing in rock friction: II Influence of relative hardness and normal load, *Int. J. Rock Mech. Min. Sci.*, *13*, 155–163.

Etchecopar, A., G. Vasseur, and M. Daignieres (1981), An inverse problem in microtectonics for the determination of stress tensors from fault striation analysis, *J. Struct. Geol.*, *3*(1), 51–65.

Fagereng, A., F. Remitti, and R. H. Sibson (2011), Incrementally developed slickenfibers – Geological record of repeating low stress-drop seismic events? *Tectonophysics*, *510*(3–4), 381–386.

Fondriest, M., S. Smith, T. Candela, S. Nielsen, K. Mair, and G. Di Toro (2013), Mirror-like faults and power dissipation during earthquakes, *Geology*, *41*(11), 1175–1178.

Giger, S., S. Cox, and E. Tenthory (2008), Slip localization and fault weakening as a consequence of fault gouge strengthening — Insights from laboratory experiments, *Earth Planet. Sci. Lett.*, *276*, 73–84.

Greenwood, J. A., and J. B. P. Williamson (1966), Contact of nominally flat surfaces, *Proc. R. Soc. Lond. A*, *295*(1442), 300–319.

Han, R., T. Hirose, T. Shimamoto, Y. Lee, and J. Ando (2011), Granular nanoparticles lubricate faults during seismic slip, *Geology*, *39*, 599–602, doi:10.1130/G31842.1.

Hertz, H. (1881), On the contact of elastic solids, *J. Reine Angew. Math.*, *92*(110), 156–171.

Hirose, T., K. Mizoguchi, and T. Shimamoto (2012), Wear processes in rocks at slow to high slip rates, *J. Struct. Geol.*, *38*(C), 102–116.

Hyun, S., L. Pei, J. F. Molinari, and M. O. Robbins (2004), Finite-element analysis of contact between elastic self-affine surfaces, *Phys. Rev. E*, *70*(2), 026117.

Johnson, K. L. (1985), Normal contact of elastic solids: Hertz theory, in *Contact Mechanics*, pp. 84–106 .

Kirkpatrick, J., C. Rowe, J. C. White, and E. E. Brodsky (2013), Silica gel formation during fault slip: Evidence from the rock record, *Geology*, *41*(9), 1015–1019, doi:10.1130/G34483.1.

Kitamura, Y., et al. (2013), Nanograins, roughness, and organic matter on a glossy fault surface with striation; an example from an exhumed subduction megasplay fault, the Nobeoka thrust, Japan. Abstract T31F-2582 presented at the Fall AGU Meeting, San Francisco.

Kitamura, Y., et al. (2005), Mélange and its seismogenic roof décollement: A plate boundary fault rock in the subduction zone—An example from the Shimanto Belt, Japan, *Tectonics*, *24*, TC5012, doi:10.1029/2004TC001635.

Kuo, L.-W., S.-R. Song, J. Suppe, and E.-C. Yeh (2016), Fault mirrors in seismically active fault zones: A fossil of small earthquakes at shallow depths, *Geophys. Res. Lett.*, *43*, 1950–1959, doi:10.1002/2015GL066882.

Means, W. D. (1987), A newly recognised type of slickenside striation, *J. Struct. Geol.*, *9*(5/6), 585–590.

Mikic, B. B., and R. T. Roca (1974), A solution to the contact of two rough spherical surfaces, *J. Appl. Mech.*, *41*(3), 801–803.

Mitchell, T. M., V. Toy, G. Di Toro, J. Renner, and R. H. Sibson (2016), Fault welding by pseudotachylyte formation, *Geology*, *44*(12), 1059–1062, doi:10.1130/G38373.1.

Niemeijer, A. R., C. J. Spiers, and C. J. Peach (2008), Frictional behaviour of simulated quartz fault gouges under hydrothermal conditions: Results from ultra-high strain rotary shear experiments, *Tectonophysics*, *460*(1–4), 288.

Otsubo, M., N. Shigematsu, K. Imanishi, R. Ando, M. Takahashi, and T. Azuma (2013), Temporal slip change based on curved slickenlines on fault scarps along Itozawa fault caused by 2011 Iwaki earthquake, northeast Japan, *Tectonophysics*, *608*(C), 970–979.

Pec, M., H. Stünitz, R. Heilbronner, M. Drury, and C. di Capitani (2012), Origin of pseudotachylites in slow creep experiments, *Earth Planet. Sci. Lett.*, *355-356*(c), 299–310.

Pei, L., S. Hyun, J. F. Molinari, and M. O. Robbins (2005), Finite element modeling of elastic-plastic contact between rough surfaces, *J. Mech. Phys. Solids*, *53*, 2385–2409.

Petit, J. P. (1987), Criteria for the sense of movement on fault surfaces in brittle rocks, *J. Struct. Geol.*, *9*(5), 597–608.

Power, W. L., and T. E. Tullis (1989), The relationship between slickenside surfaces in fine-grained quartz and the seismic cycle, *J. Struct. Geol.*, *11*(7), 879–893.

Power, W. L., T. E. Tullis, S. R. Brown, G. N. Boitnott, and C. H. Scholz (1987), Roughness of natural fault surfaces, *Geophys. Res. Lett.*, *14*(1), 29–32.

Renard, F., C. Voisin, D. Marsan, and J. Schmittbuhl (2006), High resolution 3D laser scanner measurements of a strike-slip fault quantify its morphological anisotropy at all scales, *Geophys. Res. Lett.*, *33*, L04305, doi:10.1029/2005GL025038.

Renard, F., K. Mair, and O. Gundersen (2012), Surface roughness evolution on experimentally simulated faults, *J. Struct. Geol.*, *45*(C), 101–111.

Rimstidt, J. D., and H. Z. L. Barnes (1980), The kinetics of silica-water reactions, *Geochim. Cosmochim. Acta*, *44*, 1683–1699.

Sagy, A., E. E. Brodsky, and G. J. Axen (2007), Evolution of fault-surface roughness with slip, *Geology*, *35*, 283–286, doi:10.1130/G23235A.1.

Sibson, R. H. (1989), Earthquake faulting as a structural process, *J. Struct. Geol.*, *11*(1–2), 1–14.

Sibson, R., and V. G. Toy (2006), The habitat of fault-generated pseudotachylyte: Presence vs. absence of friction melt, *Am. Geophys. Union Geophys. Monogr.*, *170*, 153–166.

Scholz, C. (1998), Earthquakes and friction laws, *Nature*, *391*, 37–41.

Smith, S., A. Billi, G. Di Toro, and R. Speiss (2011), Principal slip zones in limestone: Microstructural characterization and implications for the seismic cycle (Tre Monti Fault, Central Apennines, Italy), *Pure Appl. Geophys.*, *168*(12), 2365–2393.

Spörli, K. B., and H. J. Anderson (1990), Paleostress axes from mineral striations in faulted Mesozoic basement, Auckland, New Zealand, *N. Z. J. Geol. Geophys.*, *23*(2), 155–166.

Spray, J. G. (1992), A physical basis for the frictional melting of some rock-forming minerals, *Tectonophysics*, *204*(3–4), 205–221.

Toy, V. G., and T. Mitchell (2014), Photo of the month, *J. Struct. Geol.*, *64*(C), iii.

Toy, V. G., T. M. Mitchell, A. Druiventak, and R. Wirth (2015), Crystallographic preferred orientations may develop in nanocrystalline materials on fault planes due to surface energy interactions, *Geochem., Geophys., Geosyst.*, *16*, 2549–2563, doi:10.1002/2015GC005857.

Twiss, R. J., G. M. Protzman, and S. D. Hurst (1991), Theory of slickenline patterns based on velocity gradient tensor and microrotation, *Tectonophysics*, *186*, 215–239.

Verberne, B. A., O. Plümper, D. A. M. de Winter, and C. J. Spiers (2014), Superplastic nanofibrous slip zones control seismogenic fault friction, *Science*, *346*(6215), 1342–1344.

Wirth, R. (2004), Focused ion beam (FIB): A novel technology for advanced application of micro- and nanoanalysis in geosciences and applied mineralogy, *Eur. J. Mineral.*, *16*, 863–876.

Wojtal, S. (2001), The nature and origin of asymmetric arrays of shear surface in fault zones, *Geol. Soc. Lond. Spec. Publ.*, *186*, 171–193.